NANOSCIENCE AND TECHNOLOGY: AN INTERNATIONAL JOURNAL

ISSN Print: 2572-4258; ISSN Online: 2572-4266

Publisher- Begell House, USA.

Accepted December 29th 2020

DOUBLE DIFFUSIVE CONVECTION IN A DISSIPATIVE ELECTRICALLY CONDUCTING NANOFLUID UNDER ORTHOGONAL ELECTRICAL AND MAGNETIC FIELDS: *A NUMERICAL STUDY*

J.C. Umavathi[1*] and O. Anwar Bég[2]

[1] *Dipartimento di Ingegneria dell'Universita` degli Studi della Campania "Luigi Vanvitelli,"*
Via Roma 29, Aversa (CE), ***Italy****.* ***Email: drumavathi@rediffmail.com***

[2] *Professor of Engineering Science & Director- Multi-Physical Engineering Sciences Group, Mechanical Engineering Department, School of Science, Engineering and Environment (SEE), University of Salford, Manchester, M54WT,* ***UK. Email: O.A.Beg@salford.ac.uk / gortoab@gmail.com***

****Corresponding author***

ABSTRACT

Two-dimensional double-diffusive convective flow in a duct is studied numerically. The duct is filled with electrically conducting nanofluid and subjected to mutually orthogonal static electrical and magnetic fields. The one-phase Tiwari-Das model is employed to simulate nanoscale effects. The study is conducted for four different electroconductive nanofluids using water as a base fluid. The left and right plates of the enclosure are kept at different constant temperatures and concentrations. The top and bottom faces are insulated and impermeable to heat and mass transfer respectively. The transport equations describe the velocity, temperature and nanoparticle concentration fields. These coupled differential Navier-Stokes equations are nonlinear, and therefore discretized via a robust Finite Difference Method (FDM). The reduced difference equations are solved by incorporating the Successive-Over-Relaxation (SOR) method. The results are shown graphically for various governing parameters. The skin friction, Nusselt and Sherwood numbers for the impact of selected electromagnetic, nanoscale and thermophysical parameters are computed. The study is relevant to thermal power technologies, bioelectromagnetic therapy and nuclear engineering heat transfer control.

KEY WORDS: *Electrical field; magnetic field; conducting nanofluids; thermosolutal convection; nonlinear; viscous flow; duct; finite difference method (FDM).*

NOMENCLATURE

A	duct aspect ratio (a/b)
a	length of the duct $[m]$
b	breadth of the duct $[m]$
B_0	strength of magnetic field $[Nm/A]$ (Newton-meters per ampere)
Br	Brinkman number $\left(\dfrac{\mu_f^3}{K_f\ \rho_f^2\ b^2 (T_2 - T_1)}\right)$
C	concentration $\left[Kg\ m^{-1}\right]$
c	non-dimensional concentration
C_s	concentration susceptibility [moles]
C_P	isobaric specific heat $\left[kJ\ kg^{-1}\ K^{-1}\right]$
D	solutal diffusivity $\left[m^2/s\right]$
Df	Dufour parameter $\left(\left(\dfrac{D}{\nu}\right)_f \dfrac{K_{Tf}(C_2 - C_1)}{C_S\ C_P (T_2 - T_1)}\right)$
E_0	electric field (V/m) (volts per meter)
E	electric field load parameter
g	gravitational acceleration $\left[m/s^2\right]$
GRT	thermal Grashof number $\left(g\beta_{Tf}\Delta T\, b^3\rho_f^2/\mu_f^2\right)$
GRC	concentration Grashof number $\left(g\beta_{Cf}\Delta T\, b^3\rho_f^2/\mu_f^2\right)$
Sh	Sherwood number
Sr	Soret number $\left(\left(\dfrac{D}{\nu}\right)_f \dfrac{K_{Tf}(T_2 - T_1)}{T_m (C_2 - C_1)}\right)$
T	temperature $[K]$
T_0	reference temperature $[K]$
U, V, W	components of velocity $[m/s]$
u, v, w	dimensionless components of velocity
X, Y, Z	coordinates of space $[m]$
x, y, z	dimensionless space coordinates
Greek symbols	
α	heat diffusivity $\left[m^2 s^{-1}\right]$
β	coefficient of thermal expansion $\left[K^{-1}\right]$
σ	electrical conductivity of nanofluid $\left[s\ m^{-1}\right]$ (siemens per meter)
ρ	density of nanofluid $\left[kg/m^3\right]$
μ	dynamic viscosity of nanofluid $[kg/ms]$
ν	kinematic viscosity of nanofluid $\left[m^2/s\right]$
Φ	solid volume fraction of nanoparticles

K	thermal conductivity $\left[W\ m^{-1}\,K^{-1}\right]$	θ	dimensionless temperature
K_{Tf}	thermal diffusion ratio	***Subscripts***	
M	Hartmann number $\left(B_0^2\ b^2\ \sigma_f/\mu_f\right)$	1	left wall
Pr	Prandtl number $\left(\nu/\alpha\right)_f$	2	right wall
Q	volumetric flow rate	nf	nanofluid
Sc	Schmidt number $\left(\nu/D\right)_f$	f	base fluid
		s	solid nanoparticles

1. INTRODUCTION

The interest in the deployment of externally applied magnetic fields has been an active area of sciences for over half a century. Such flows find important applications in nuclear power control, magnetic materials processing, electromagnetic propulsion systems, bio-electromagnetics in medicine and many other fields.

Many different phenomena can be controlled and examples include magnetic induction in polymer alignment, texturing of materials during a phase transition in both liquid-to-solid and solid-to-solid state transitions, magnetic levitation of diamagnetic matter, texture development in metals and damping of magnetic fields on conductive liquids. The MHD effects are implemented in industries and technical systems to influence and control the flow of liquid metals. Malashetty *et al.* (2006) investigated the flow characteristics of conducting immiscible fluids in a vertical enclosure. Later Umavathi *et al.* (2011, 2013a, 2014a, 2016a, 2017c) studied the dynamics of viscous electrically conducting fluids in ducts and channels using boundary conditions of the first and third kind, energy and chemical reaction of not miscible fluids and also movable baffle interactional MHD flows.

Double-diffusive (thermosolutal) natural convection is an important type of free convection in which buoyancy force consists of two components with different rates of diffusion. In other words, buoyancy force is imposed by both temperature and concentration gradients. Double-diffusive MHD convection is significant for material solidification processes (Younsi, 2009) and in hydro-magnetic lubrication, smart coating synthesis, purification of molten metals, rolling, etc. (Sharma and Singh, 2009, Vadher et al. 2010). Trevisan and Bejan (1987) researched the natural convection including the temperature and concentration thermal effects Lee and Hyun (1990) considered the double-diffusive convection in a cavity with opposing horizontal concentration and temperature gradients. Be´ghein et al. (1992) numerically proposed correlations characterizing both heat and mass transfer rates. The unsteady free convection for the influence of Soret and Dufour in the enclosure was detailed by Wang *et al*. (2014).

Nanofluids can therefore be considered to be the next-generation working fluids in modern heat transfer technologies. Highly efficient heat transfer enhancement techniques are urgently needed in engineering and nanofluids offer a robust strategy in this regard, even if there still remain a number of uncertainties in their thermophysical properties estimations (Yu et al. 2008, Minea, 2014, Ting et al. 2014, Aybar, 2015). It has been claimed (Wang and Mujumdar, 2007) that convective heat transfer enhancement is due mainly to *dispersion* of the suspended nanoparticles, and partly due to intensification of turbulence by nanoparticles (Xuan and Li, 2003). However, the careful theoretical consideration and data analysis made by Buongiorno (2006) revealed that such dispersion is negligible, and that turbulence is not detracted by the presence of nanoparticles. Using Buongiorno's model, Umavathi and collaborators (2013b, 2014c, 2016b, 2017a) analysed the onset of convection adopting Darcy model and thermal modulation in a nanofluid saturated porous layer. Using the single-phase nanofluid model Umavathi *et al.* (2016c, 2017c, 2018) discussed heat transfer using variable properties. Recently Diglio *et al*. (2018) for the first time in the literature investigated borehole heat exchangers utilizing nanofluids as heat carriers.

Magnetic nanoparticles are added to a base fluid such as hydrocarbon oil, diesel oil, kerosene, water etc. to obtain good control on the characteristics of fabricate magnetic nanofluids (MNF). The nanoparticles aggregate in the presence of magnetic field generating high conductivity which helps to raise the thermal conductivity of the magnetic nanofluids. Motivated by such applications, in the current study, a detailed numerical study is demonstrated for the double-diffusive (thermosolutal) natural convection in a vertical rectangular duct. The duct is filled with electrically conducting nanofluid and subjected to mutually orthogonal static electrical and magnetic fields. The one-phase Tiwari-Das model is employed to simulate nanoscale effects. The study is conducted for four different electroconductive nanofluids using water as base fluid. The well known Boussinesq approximation is adopted.

The non-dimensional conservation equations are strongly nonlinear and are solved employing numerical technique i.e. the Finite Difference Method (FDM). To get convergent solutions the Successive-Over-Relaxation (SOR) method along with Gauss-Seidal method is implemented to solve the reduced difference equations. Extensive visualization of solutions is presented graphically for velocity, temperature, nanoparticle concentration, Nusselt number , shear stress and Swearword numbers for the impact of selected electrical, magnetic, nanoscale and thermophysical parameters.

2. MATHEMATICAL FORMULATION

The electromagnetic nanofluid duct thermosolutal convection regime under consideration is visualized in Fig. 1. Induced magnetic field produced by the motion of an electrically conducting fluid is negligible compared to the applied magnetic field. Uniform electric field E_0 is applied along the $X-$direction and a uniform magnetic field B_0 is applied along the $Y-$direction which is normal to the $X-$direction. The left wall of the duct is heated at a constant temperature T_1 having concentration C_1 and the right wall is heated at a constant temperature T_2 possessing concentration C_2 such that right wall is always at a higher temperature in comparison with the left wall and also $C_2 > C_1$ as shown in Fig. 1. The temperature difference causes a temperature gradient which is the source of buoyancy force. This gradient is normal to the body force which is a gravitational force (Oberbeck convection) and therefore the flow inside the duct occurs only due to buoyancy force and not the pressure gradient. Hence the pressure gradient is not included in the mass conservation equation. Further the flow is *fully developed* and hence derivatives of velocity i.e. $X \left(\frac{\partial U}{\partial X}\right)$ and $Y \left(\frac{\partial V}{\partial Y}\right)$ terms vanish. Hall current, Maxwell displacement and ion slip effects are ignored.

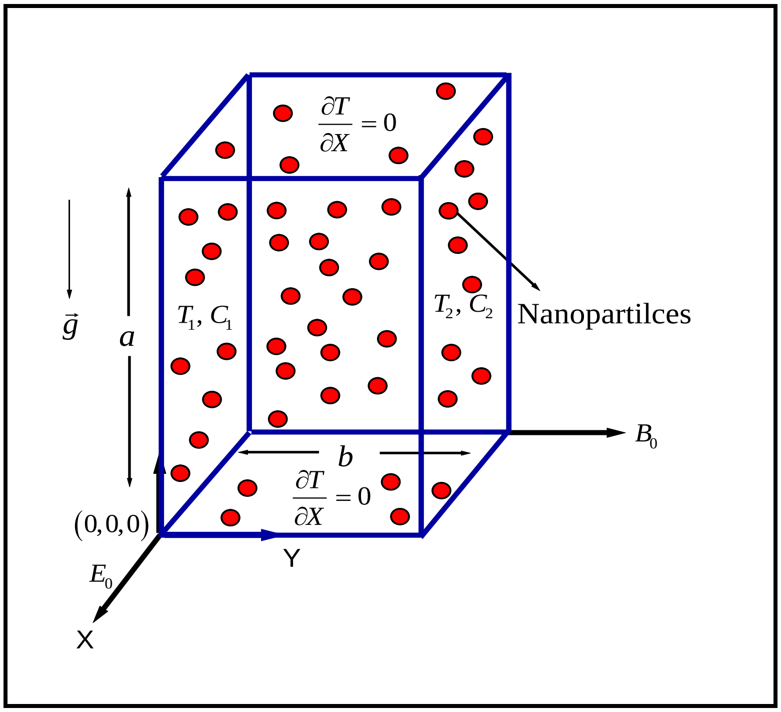

FIG. 1: Physical configuration.

Implementing the above assumptions, the governing equations in dimensionless form become

$$\frac{\partial^2 w}{\partial x^2}+\frac{\partial^2 w}{\partial y^2}+GRT\,(1-\Phi)^{2.5}\left(1-\Phi+\Phi\frac{(\rho\beta)_s}{(\rho\beta)_f}\right)\theta\;-\left(1-\Phi+\Phi\frac{(\rho\beta)_s}{(\rho\beta)_f}\right)C$$
$$GRC\,(1-\Phi)^{2.5}\;C-M^2\;(1-\Phi)^{2.5}\;\frac{\sigma_{nf}}{\sigma_f}\;w+\;M^2\,E\;(1-\Phi)^{2.5}\;\frac{\sigma_{nf}}{\sigma_f}\;=0 \tag{1}$$

$$\frac{\partial^2\theta}{\partial x^2}+\frac{\partial^2\theta}{\partial y^2}+\frac{Br}{(1-\Phi)^{2.5}}\left(\frac{K_s+2K_f+\Phi(K_f-K_s)}{K_s+2K_f-2\Phi(K_f-K_s)}\right)\left(\left(\frac{\partial w}{\partial x}\right)^2+\left(\frac{\partial w}{\partial y}\right)^2\right)+$$
$$\frac{D_f\;\Pr\;K_f}{K_{nf}\;(\rho C_p)_f}\left(\frac{\partial^2 c}{\partial x^2}+\frac{\partial^2 c}{\partial y^2}\right)+Br\;M^2\;\frac{\sigma_{nf}}{\sigma_f}\left(\frac{K_s+2K_f+\Phi(K_f-K_s)}{K_s+2K_f-2\Phi(K_f-K_s)}\right)(E-w)^2=0 \tag{2}$$

$$\frac{\partial^2 c}{\partial x^2}+\frac{\partial^2 c}{\partial y^2}+Sr\;\;Sc\;\left(\frac{\partial^2\theta}{\partial x^2}+\frac{\partial^2\theta}{\partial y^2}\right)=0 \tag{3}$$

The corresponding dimensionless prescribed boundary conditions take the following form:

$$
\begin{array}{llllll}
w=0, & \theta=-0.5, & c=-0.5 & \text{at} & y=0 & \text{for } 0\le x\le A \\
w=0, & \theta=0.5, & c=0.5 & \text{at} & y=1 & \text{for } 0\le x\le A \\
w=0, & \dfrac{\partial\theta}{\partial x}=0, & \dfrac{\partial c}{\partial x}=0 & \text{at} & x=0 \text{ and } x=A & \text{for } 0\le y\le 1
\end{array}
\tag{4}
$$

In the above equations, the following nondimensional parameters are used:

$$
x=\frac{X}{b},\ y=\frac{Y}{b},\ w=\frac{W\rho_f b}{\mu_f},\ \theta=\frac{(T-T_0)}{(T_2-T_1)},\ c=\frac{(C-C_0)}{(C_2-C_1)},\ T_0=\frac{(T_1+T_2)}{2},
$$

$$
C_0=\frac{(C_1+C_2)}{2},\quad GRT=\frac{g\beta_{Tf}(T_2-T_1)b^3\rho_f^2}{\mu_f^2},\ GRC=\frac{g\beta_{Cf}(C_2-C_1)b^3\rho_f^2}{\mu_f^2},
$$

$$
M^2=\frac{B_0^2\ b^2\ \sigma_f}{\mu_f},\ E=\frac{E_0\, b\,\rho_f}{B_0\ \mu_f},\ Br=\frac{\mu_f^3}{K_f\ \rho_f^2\ b^2(T_2-T_1)},\ \alpha=\frac{K_f}{(\rho C_p)_f},
$$

$$
\Pr=\left(\frac{\nu}{\alpha}\right)_f,\ Df=\left(\frac{D}{\nu}\right)_f\frac{K_{Tf}(C_2-C_1)}{C_S\ C_P(T_2-T_1)},\ Sr=\left(\frac{D}{\nu}\right)_f\frac{K_{Tf}(C_2-C_1)}{T_m(T_2-T_1)},\ Sc=\left(\frac{\nu}{D}\right)_f
\tag{5}
$$

The properties of nanofluid can be defined based on the properties as

$$(\rho)_{nf}=(1-\Phi)\rho_f+\Phi\rho_s \tag{6}$$

$$(\rho C_p)_{nf}=(1-\Phi)(\rho C_p)_f+\Phi(\rho C_p)_s \tag{7}$$

$$(\rho\beta)_{nf}=(1-\Phi)(\rho\beta)_f+\Phi(\rho\beta)_s \tag{8}$$

$$\alpha_{nf}=\frac{K_{nf}}{(\rho C_p)_{nf}} \tag{9}$$

The effective dynamic viscosity, effective electrical conductivity and thermal conductivity for the spherical nanoparticle following Brinkman (1952), Sheikholeslami *et al.* (2013) and Maxwell (1904) are:

$$\mu_{nf}=\frac{\mu_f}{(1-\Phi)^{2.5}} \tag{10}$$

$$\frac{\sigma_{nf}}{\sigma_f}=(1-\Phi)+\Phi\left(\frac{\sigma_s}{\sigma_f}\right) \tag{11}$$

$$K_{nf}=K_f\left(\frac{K_s+2K_f-2\Phi(K_f-K_s)}{K_s+2K_f+\Phi(K_f-K_s)}\right) \tag{12}$$

The physical characteristics such as volumetric flow rate, Nusselt number, skin friction and Sherwood number are evaluated using copper as the nanoparticle and water as a base fluid and shown in Tables 2 - 4.

The local Nusselt number and Sherwood number is computed at each section of the hot surfaces using the following equation.

$$\overline{Nu} = -\frac{K_{nf}}{K_f}\frac{\partial \theta}{\partial y},\ Sh = -\frac{K_{nf}}{K_f}\frac{\partial c}{\partial y} \tag{13}$$

The average Nusselt number is evaluated by dividing the integrated local Nusselt number along the heated plate by the length of the heated plate of the enclosure. Thus, the average rate heat transfer across the whole domain can be estimated by the following expression:

$$Nu = \frac{1}{A}\sum_{i=1}^{100}\int_{x_{2i}}^{x_{2i+1}} \overline{Nu}\ dX \tag{14}$$

Similarly, the skin friction and volumetric flow rate are evaluated.

3. COMPUTATIONAL FINITE DIFFERENCE METHOD (FDM) SOLUTION

The system of governing Eqns. (1) - (3), in conjunction with the boundary conditions as defined in Eqn. (4), are solved through the application of a finite difference method. Uniform grids are generated for the computational domain. The domain of definition is portioned uniformly into Nx and Ny divisions along the x and y axes respectively. Central differencing of second-order accuracy is employed for the first and second order derivatives. Therefore, the resultant difference equations become:

$$\frac{w_{i+1,j} - 2w_{i,j} + w_{i-1,j}}{(\Delta x)^2} + \frac{w_{i,j+1} - 2w_{i,j} + w_{i,j-1}}{(\Delta y)^2} + GRT(1-\Phi)^{2.5}\left(1 - \Phi + \Phi\frac{(\rho\beta)_s}{(\rho\beta)_f}\right)\theta_{i,j} -$$
$$GRC(1-\Phi)^{2.5}\left(1 - \Phi + \Phi\frac{(\rho\beta)_s}{(\rho\beta)_f}\right)c_{i,j} - M^2(1-\Phi)^{2.5}\frac{\sigma_{nf}}{\sigma_f}w_{i,j} +$$
$$M^2E(1-\Phi)^{2.5}\frac{\sigma_{nf}}{\sigma_f} = 0 \tag{15}$$

$$
\begin{aligned}
&\frac{\theta_{i+1,j}-2\theta_{i,j}+\theta_{i-1,j}}{(\Delta x)^2}+\frac{\theta_{i,j+1}-2\theta_{i,j}+\theta_{i,j-1}}{(\Delta y)^2}+\\
&\frac{Br}{(1-\Phi)^{2.5}}\left(\frac{K_s+2K_f+\Phi(K_f-K_s)}{K_s+2K_f-2\Phi(K_f-K_s)}\right)\left(\left(\frac{w_{i+1,j}-w_{i-1,j}}{2\Delta x}\right)^2+\left(\frac{w_{i,j+1}-w_{i,j-1}}{2\Delta y}\right)^2\right)\\
&\frac{D_f\ \Pr\ K_f}{K_{nf}\ (\rho C_p)_f}\left(\frac{c_{i+1,j}-2c_{i,j}+c_{i-1,j}}{(\Delta x)^2}+\frac{c_{i,j+1}-2c_{i,j}+c_{i,j-1}}{(\Delta y)^2}\right)+\\
&Br\ M^2\ \frac{\sigma_{nf}}{\sigma_f}\left(\frac{K_s+2K_f+\Phi(K_f-K_s)}{K_s+2K_f-2\Phi(K_f-K_s)}\right)(E-w_{i,j})^2=0
\end{aligned}
\tag{16}
$$

$$
\begin{aligned}
&\frac{c_{i+1,j}-2c_{i,j}+c_{i-1,j}}{(\Delta x)^2}+\frac{c_{i,j+1}-2c_{i,j}+c_{i,j-1}}{(\Delta y)^2}+\\
&Sr\ \ Sc\left(\frac{\theta_{i+1,j}-2\theta_{i,j}+\theta_{i-1,j}}{(\Delta x)^2}+\frac{\theta_{i,j+1}-2\theta_{i,j}+\theta_{i,j-1}}{(\Delta y)^2}\right)=0
\end{aligned}
\tag{17}
$$

The corresponding discretized conditions on the boundary are:

$$
\begin{aligned}
&w_{i,0}=-w_{i,1},\ \theta_{i,0}=-1-\theta_{i,1},\ \ c_{i,0}=-1-c_{i,1}\\
&w_{i,\,N\,y+1}=-w_{i,\,N\,y},\ \theta_{i,N\,y+1}=1-\theta_{i,\,N\,y},\ \ c_{i,\,N\,y+1}=1-c_{i,\,N\,y}\\
&w_{0,\,j}=-w_{1,\,j},\ \theta_{0,\,j}=\theta_{1,\,j},\ \ c_{0,\,j}=c_{1,\,j}\\
&w_{N\,x+1,\,j}=-w_{N\,x,\,j},\ \theta_{N\,x+1,j}=\theta_{N\,x,\,j},\ \ c_{N\,x+1,\,j}=c_{N\,x,\,j}
\end{aligned}
\tag{18}
$$

The resultant algebraic equations i.e. Eqns. (15) to (17) are solved iteratively using Gauss-Seidel method. Southwell-Over-Relaxation is implemented for the convergence criteria. A detailed description of the numerical procedure is provided in Umavathi *et al*. (2011).

3.1 Grid measurement and code validation: To verify the grid independence, numerical experiments are performed as shown in Table-1. Different mesh sizes are used. The Nusselt number is calculated at the cold and hot walls to fix the grid size for the computations. Table 1 suggests that a 100×100 grid size is sufficient. The computations are terminated when the values satisfy the condition $\left|\Gamma^{n+1}-\Gamma^{n}\right|<10^{-14}$ (n is the iteration number and Γ denotes W and θ and n represent the number of the iteration).

4. RESULTS AND DISCUSSION

The results are depicted in terms of the impact of using different nanoparticles such as copper, alumina and titanium oxide using water as base fluid, Hartman number $\left(0 \leq M \leq 2\right)$, electric field load parameter $\left(-1 \leq E \leq 1\right)$, thermal Grashof number $\left(-10 \leq GRT \leq 10\right)$, concentration (solutal) Grashof number $\left(5 \leq GRC \leq 15\right)$, solid volume nanoparticle fraction $\left(0 \leq \Phi \leq 0.05\right)$, Brinkman number $\left(0 \leq Br \leq 0.1\right)$ and Dufour parameter $\left(0 \leq Df \leq 1\right)$. The plots for the impact of these parameters are presented graphically in Figs. 2 to 9. The Figs. 3 to 9 and the tabulated values are drawn using copper as nanoparticle and base fluid as water. To plot all graphs and compute tables, the nondimensional parameters are selected as: $M = 2,\ E = -1,\ GRT = 10, GRC = 5,\ \Phi = 0.05,\ Br = 0.1,\ \Pr = 7, Df = 1,\ Sr = 0.5,\ Sc = 0.5,$ except the varying parameter. The figures are drawn in three dimensions (3D), two dimensions (2D) and in one dimension (1D) using Matlab software. One dimensional graphs correspond to $y = 0.5$ with x varying from 0 to 1. To appreciate the shape of the flow in a more comprehensive fashion, these different visualizations provide different perspectives. Further the values assigned to the electric field load parameter are $E = \pm 1$ and $E = 0$ which suggest the case of an *open circuit* and *short circuit*, respectively.

The effect of using different nanoparticles (copper, alumina and titanium oxide) on the velocity, energy and concentration fields are portrayed in Fig. 2. It is evident that the velocity variations are in the downward direction of the duct (3D) and the magnitude for copper and alumina are similar whereas the deepening in the downward direction is more pronounced in the case of titanium oxide as the suspension in the base fluid (Fig. 2a). The 2D presentation does not infer any further insight into the velocity contours. The 3D and 2D temperature profiles can be viewed in Fig. 2b. The temperature distribution in 3D shows that the disk takes the position of the convexity and the contours for copper are more nonlinear in comparison with alumina and titanium oxide. Figure 2c demonstrate the concentration distribution and the topology is in concave position (opposite to temperature) and the contours are much less disturbed for all the nanoparticles. Figure 2d (1D) reveals that copper achieves the maximum velocity and titanium oxide produces the minimum velocity magnitude i.e. flow acceleration is greatest in the case of copper-nanofluid. Figure 2e indicates that the temperature is minimized for titanium oxide and maximized for copper nanoparticle and the opposite effect is seen in the case of the nanoparticle concentration (Fig. 2f).

The influence of magnetic field on the flow are presented in Fig. 3. Figure 3a implies that in the absence of applied magnetic field ($M = 0$) the upward $\left(\frac{1}{2} < y < 1\right)$ and downward $\left(0 < y < \frac{1}{2}\right)$ flows are symmetric (3D) whereas in the presence of magnetic field the upward flow is reduced in comparison with $M = 0$ and the downward flow increases as M increases (3D) i.e. there is evidently a *re-distribution in momentum* in the duct due to magnetic field effect. Further Fig. 3a also depicts that symmetrical convection circulations are obtained that occupy equal zones both in the upper half region $\left(\frac{1}{2} < y < 1\right)$ and in the lower half region $\left(0 < y < \frac{1}{2}\right)$ in the *absence of magnetic field and there are two cells*. In the presence of applied magnetic field only *one cell* is produced and the number of circulations are increased with increasing M (2D). Therefore, the intensity of upward flow is reduced with stronger magnetic field. It is apparent from Fig. 3d that the velocity is *linear* without the magnetic force whereas it decreases as magnetic field increases. Moreover the magnetic field is applied perpendicular to the vertical axis; consequently, the magnetic force interacts with the buoyancy force as well as fluid motion. As a result, the intensity of circulation declines for rising magnetic force which indicates that higher magnetic force diminishes the convective force inside the enclosure. This is physically attributable to the contribution of the applied magnetic field which mobilizes a Lorentz force which acts against the buoyant force and retards the fluid motion within the duct. Without the magnetic forces, the temperature distribution is almost constant and for increasing values of Hartmann number the profiles assume a concave shape i.e. temperature bulges outside as M increases (3D picture of Fig. 3b). The energy contours for $M = 0$ (2D picture of 3b) show a similar response and decrease linearly from the upper side $(y = 1)$ to the lower side $(y = 0)$. For the values of $M = 1, 2$ the energy contours appear nonlinear and the optimum temperature is attained at the upper region owing to the improvement of the effect of work dissipated as thermal energy in dragging the nanofluid against the magnetic field. The higher the value of M, the larger the maximum temperature. For small values of M, heat flows from the upper wall to the fluid and from fluid to the lower wall since the effect of Ohmic heating is not very strong.

However, the heat may flow from the fluid region to both the upper and lower walls for large values of M. Inspection of Fig. 3e (1D) shows further that as M increases, nanofluid temperature increases and becomes progressively more nonlinear. The concentration contours depict exactly the opposite trend (Fig. 3c and 3f) to those exhibited by temperature. It means that the shape become convex for large values of M, the concentration contours look similar and are linear for any values of M and Fig. 3f indicates that as M increases the concentration distribution decreases.

Figures 4 depict the influence of electric field load parameter on the flow filed. The 3D contours (Fig. 4a) on velocity indicate that when $E = -1$, the flow is *downward* $\left(0 < y < \frac{1}{2}\right)$, when $E = 0$ (vanishing electrical field), the flow is *symmetric* with respect to downward and upward directions and for $E = 1$ the flow is *upward* $\left(\frac{1}{2} < y < 1\right)$. The 2D contours appear similar for $E = -1$ and $E = 1$ producing *only one cell* whereas for $E = 0$, there are *two cell formations* and the contours are *antisymmetric* at the midsection of the duct at $y = 0.5$. From Fig. 4d, it is evident that as E increases velocity increases (for $E = -1$ the profile is downward, for $E = 0$, the velocity is stagnant and for $E = 1$, the profile is upward) at $y = 0.5$ for the variations x. Therefore one can conclude that negative values of E intensify the downward flow, positive values of E intensify the upward flow and symmetric flow is obtained without the electric current. Figure 4b suggest that the temperature distributes convexly for $E = \pm 1$ and is almost linear for $E = 0$. The 2D contours tells that the temperature distribution is nonlinear and are similar for $E = \pm 1$. The maximum temperature is attained *in the presence of electric current (E ≠ 0)*. Figure 4e (1D) implies that the energy is high for $E = -1$ when compared with $E = 1$ at $y = 0.5$. The temperature increases due to the occurrence of Ohmic heating. The occurrence of Ohmic and viscous heating in the energy equation leads to a dominance over the buoyancy forces and therefore the temperature is elevated. The concentration distribution as seen in Figs. 4c and 4f display exactly the opposite property as that on temperature. The 3D topology is *concave for the open circuit* whereas it is *linear for short circuit;* additionally the 2D contours are not tangibly influenced by the magnetic force, and 1D profile showcases that the concentration is minimal for $E = -1$ and is linear for $M = 0$.

Figures 5a and 5b present the impact of thermal Grashof number GRT on transport characteristics. The values are chosen as $GRT = -10$ (buoyancy opposing flow), $GRT = 0$ (absence of buoyancy force i.e. forced convection) and $GRT = 10$ (buoyancy assisting flow. The 3D contours depict that for any values of GRT the flow is downward. This trend is due to these plots corresponding to $E = -1$. As observed in Fig. 4, the flow is downward for $E = -1$ and upward for $E = 1$. The 2D contours suggest that for all values of GRT only one cell is generated. Fig. 5b shows a *convex* curvature and the contours are nonlinear on GRT. Fig. 5c is *concave* for the concentration distribution and the contours (2D) are almost linear. It is clear from Fig. 5d and 5e that as GRT raises, momentum and energy fields are enhanced in the core zone of the duct. The temperature is enhanced with augmenting thermal Grashof number. The profiles of concentration are however decreased with increment in the buoyancy force (Fig. 5f). The raise in GRT causes the accentuation in buoyancy forces and therefore the momentum is enhanced which also helps to increase the temperature through viscous and Ohmic dissipations.

Figure 6 show the influence of concentration Grashof number. The plots of 3D and 2D on the velocity, temperature and concentration show a similar nature to that of GRT and hence are omitted. The 1D graph (Fig. 6) show that as GRC increases, there is enhancement in both the velocity and temperature; however the nanoparticle concentration magnitudes are reduced with increasing GRC.

Figure 7a presents the velocity evolution for different concentrations of nanoparticles. From Fig. 7a (3D), it can be viewed that flow increases in the downward direction for increasing values of solid volume fraction. Since $E = -1$ the flow is downward only. The 2D contours becomes enlarged by increasing the concentration of the nanoparticles (percentage doping of the base fluid) and also the contour density is intensified. However, with or without nanoparticles there is only one cell produced. The physical explanation for this is that increasing the solid concentration in the carrier fluid increases the density of the carrier fluid which damps the motion of nanofluid. In the present regime, it is observed that the flow is promoted with the raise in solid volume fraction in the downward direction. Hence one can conclude that the velocity is suppressed by adding the nanoparticles i.*e. flow deceleration is induced*. The temperature and concentration contours resemble those computed with a variation in thermal Grashof number and are therefore not presented. That is, the topology exhibits a convex curve nature in the temperature field whereas the concentration filed shows a concave curve pattern (3D). The 1D graph (Fig. 7b, 7c, 7d) suggest that the velocity and concentration fields decreases for increasing the sold volume fraction ϕ. The temperature is demonstrably boosted with increasing nanoparticle concentration.

The influence of Brinkman number Br on the flow characteristics are depicted in Fig. 8. The velocity, temperature and concentration contours are similar to that of GRT and therefore not shown. Figure 8 a,b,c (1D) clearly indicates that both the momentum and energy fields are promoted. This behavior is generated due to the fact that an increase in Brinkman number increases the viscous dissipation (conversion of kinetic energy into thermal energy) which helps to enhance the buoyancy forces. The upsurge of buoyancy forces leads to enlarge the velocity and hence due to the coupling effect the temperature is also elevated. The concentration decreases however markedly with an increase in Brinkman number.

The impact of Dufour number is portrayed in Fig. 9. The velocity, energy and solutal contours are similar to GRT and hence are not presented. When viewed at a single point (Figs 9 a,b,c), it is evident that the momentum and thermal profiles are being depleted whereas the concentration profiles are being enlarged. The plots of velocity, temperature and concentration with a change in Soret (thermo-diffusive) number and Schmidt parameters show a similar nature to that computed with a change in Dufour parameter and are therefore excluded for brevity.

For purely viscous fluid $(\Phi = 0)$ the present results agree with Umavathi *et al.* [4] and for duct filled with nanofluid without magnetic and electric forces the computations agree with the results of Umavathi *et al*. (2016).

The engineering design characteristics for the flow i.e. volumetric flow rate Q, skin friction along $y-$axis $\left[\frac{dw}{dy}\right]_{y\,=\,0,1}$, skin friction along $x-$axis $\left[\frac{dw}{dx}\right]_{x\,=\,0,1}$ and rate of heat transfer $\left[\frac{d\theta}{dy}\right]_{y\,=\,0,1}$ are evaluated for all the controlling parameters and tabulated in Tables 2 and 3. It is evident that titanium oxide nanoparticles produce a reduced volumetric flow rate whereas silver nanoparticles achieve a superior volumetric flow rate compared with copper and alumina nanoparticles. Further Table 2 also demonstrates that volumetric flow rate is amplified with greater values of E, GRT, GRC, Br, Df whereas it is suppressed with increasing values of M, ϕ.

The skin friction $\left[\frac{dw}{dy}\right]_{y=0}$ is a maximum for silver and a minimum for titanium oxide nanoparticles. It is boosted with increasing concentration Grashof number, Dufour numbers and depressed with increasing Hartmann, electric field load and thermal Grashof numbers. The skin friction $\left[\frac{dw}{dy}\right]_{y=1}$ upsurges for the silver nanoparticle case whereas it is decreased for titanium oxide nanoparticles. The skin friction is enlarged for higher values of M, GRC, Φ and is depleted with increment in E, GRT, Br, Df. The shear stress $\frac{dw}{dx}$ at $x = 0$ and $x = 1$ attain an upper limit for silver and a lower limit for titanium oxide nanoparticles. The skin friction at $x = 0$ is boosted with an increase in GRT, GRC, Br, Df whereas it is reduced with an elevation in M, E, Φ. At $x = 1$ the values are exactly the same as those obtained at $x = 0$ with a change in the polarity. The heat transfer rate $\frac{d\theta}{dy}$ i.e. Nusselt number, at $y = 0$ attains a maximum for silver and minimum for titanium oxide and the opposite trend is computed at $y = 1$. A rise in electric field load parameter and nanoparticle concentration Grashof number decrease Nusselt number whereas it is magnified with increasing thermal Grashof number at both walls. A boost in the parameters M, ϕ, Br, Df amplifies the Nusselt number at $y = 0$ and the opposite trend is obtained at $y = 1$. The effect of all the parameters on the Sherwood number is presented in Table 4 and a much less prominent influence is computed compared with heat transfer rate (Nusselt number).

5. CONCLUSIONS

The buoyancy-driven thermosolutal nanofluid convection in the presence of orthogonal applied electric and magnetic fields within a rectangular duct with viscous dissipation has been studied using a Tiwari-Das single-phase nanoscale approach. Cross diffusion effects have been included. The main findings of the numerical simulations are as follows:

(i)The profiles are convex for the velocity and thermal fields and concave for the concentration field. The velocity and thermal transfer is optimum for copper and lowest for titanium oxide nanoparticles and the opposite behavior is obtained for the concentration distribution.

(ii)In the absence of applied magnetic and electric fields, symmetric flow is generated both in the upward and downward flow in the duct. The presence of magnetic force results in a scale down in the velocity and concentration whereas it amplifies temperatures. The potentiality of the electric circuit has a significant effect on flow distribution – it results in acceleration in the downward flow $\left(E=-1\right)$, in the upward flow $\left(E=1\right)$, symmetric flow $\left(E=0\right)$, a spike in energy for the open circuit $\left(E=\pm 1\right)$ and a linear distribution for the short circuit $\left(E=0\right)$. The concentration distribution exhibits the opposite response to temperature distribution.

(iv) An elevation in thermal and concentration Grashof numbers and Brinkman number elevates the velocity and temperature magnitudes whereas it suppresses the concentration. Nanoparticle solid volume fraction depletes the velocity and concentration whereas it enhances the temperature. Increasing Dufour, Soret and Schmidt numbers reduce the velocity and temperature whereas they enhance concentration.

(viii) The skin friction is enhanced with higher concentration Grashof number, Dufour numbers whereas it is depressed with larger Hartmann, electric field parameter, thermal Grashof number, and solid volume fraction at the left wall. At the right wall skin friction is however accentuated with greater Hartmann (magnetic body force) number, concentration Grashof number and solid volume fraction and is depleted with the remaining parameters.

(ix) Silver nanoparticles achieve the maximum rate of heat transfer (Nusselt number) whereas titanium oxide nanoparticles produce the minimum. Nusselt number is enhanced with Hartmann number, thermal Grashof number, solid volume fraction, Brinkman number and Dufour number whereas it is reduced with greater electric field parameter and concentration Grashof number *at the left wall* of the duct. The contrary response is computed at the right wall.

The present study do not consider the non-Newtonian effects (Uddin et al. 2016, Anwar et al. 2019). These may be considered in future simulations.

(a)

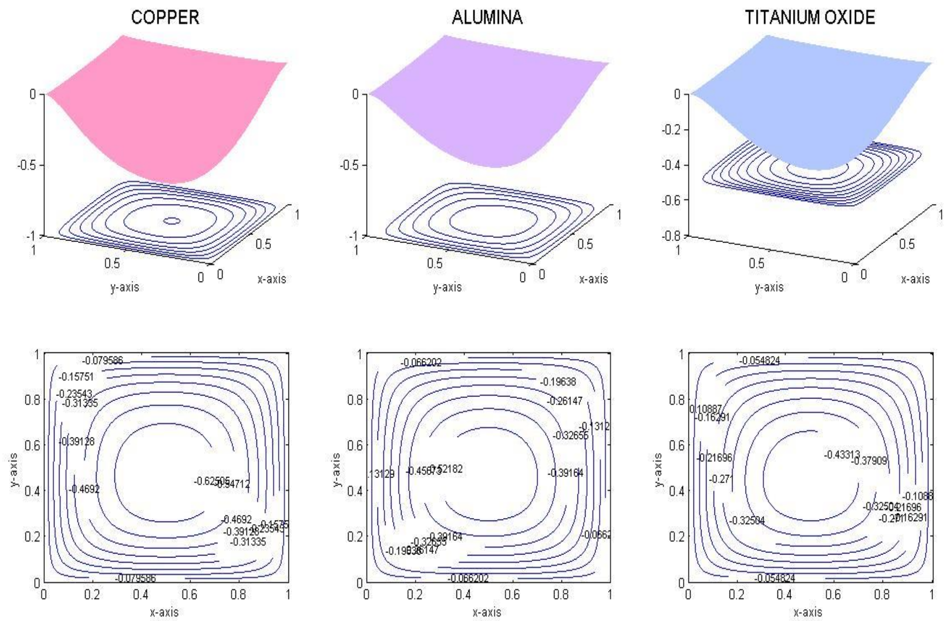
COPPER
ALUMINA
TITANIUM OXIDE
y-axis
x-axis

(b)

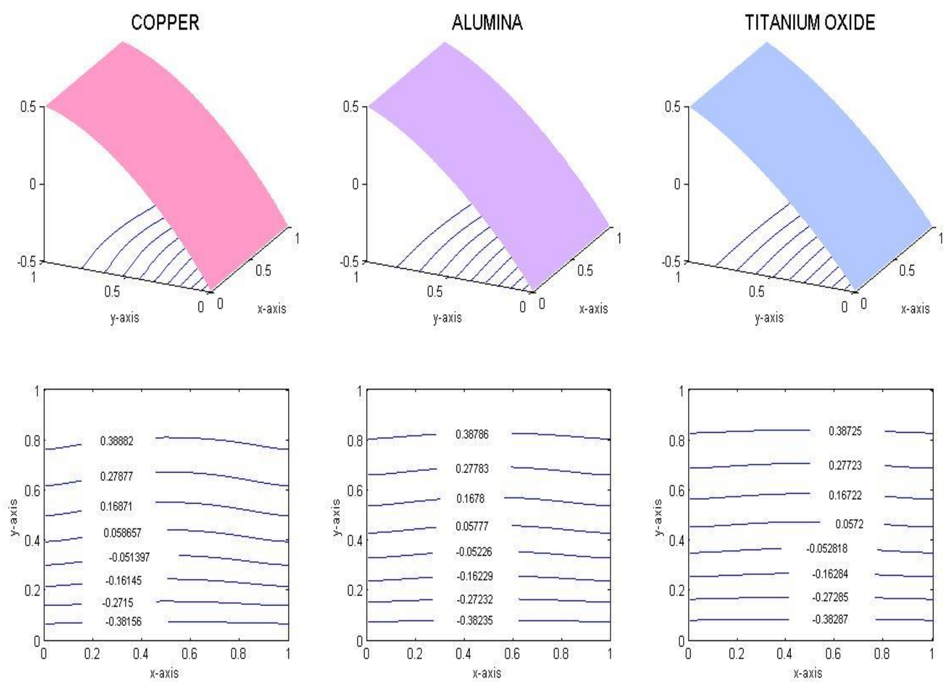
COPPER
ALUMINA
TITANIUM OXIDE
y-axis
x-axis

(c)

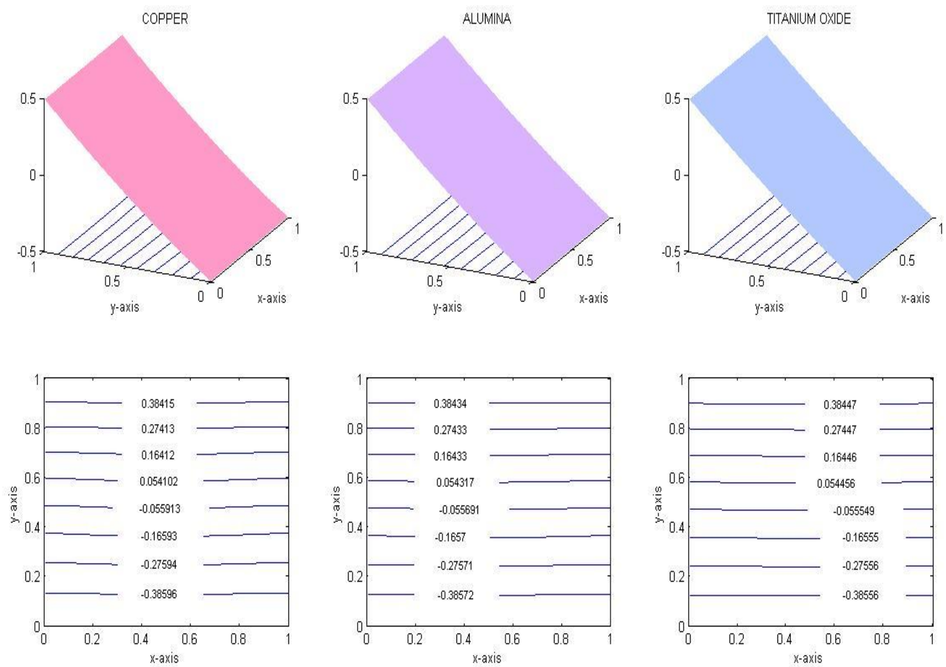

(d) **(e)** **(f)**

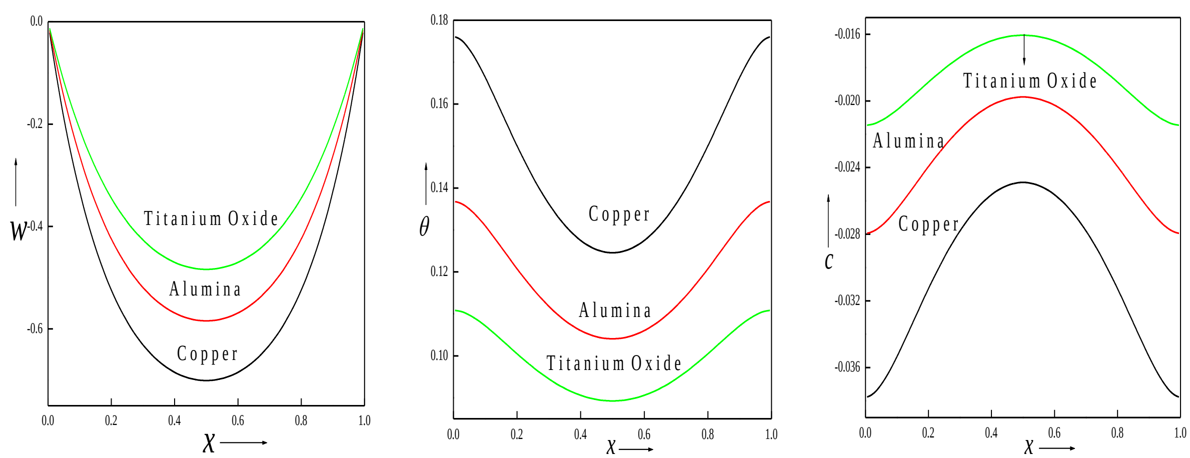

FIG. 2: Velocity (a,d), temperature (b,e) and concentration (c,f) contours and profiles respectively for different nanoparticles

(a)

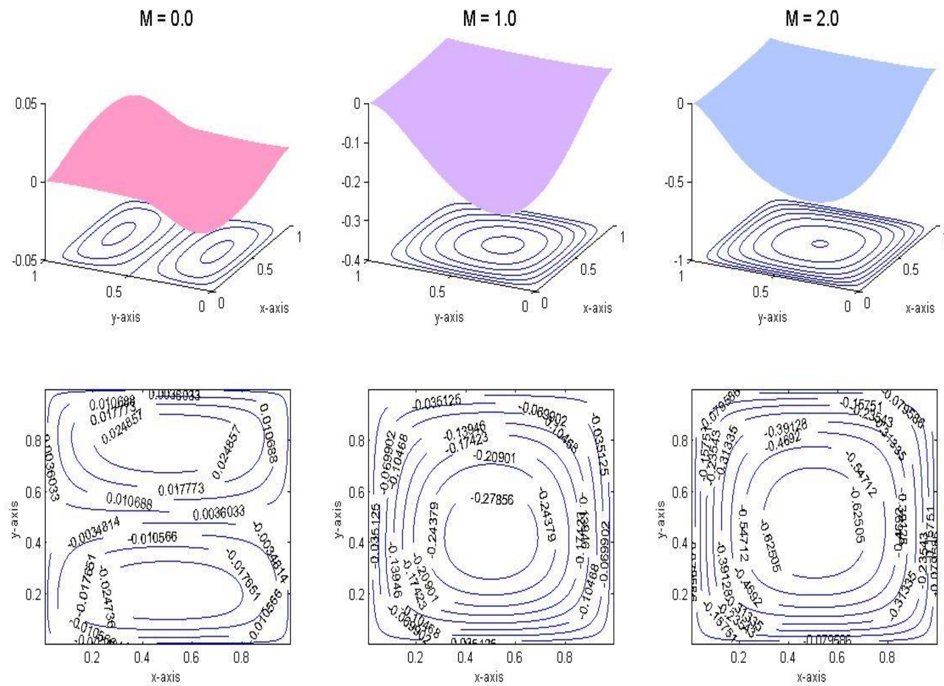
M = 0.0
M = 1.0
M = 2.0
y-axis
x-axis

(b)

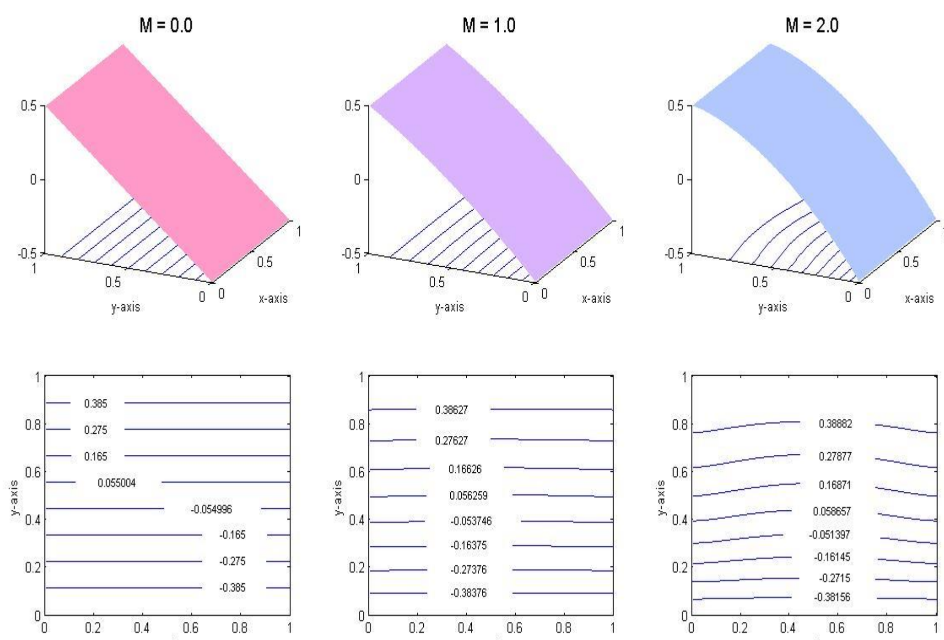
M = 0.0
M = 1.0
M = 2.0
y-axis
x-axis
0.385
0.275
0.165
0.055004
-0.054996
-0.165
-0.275
-0.385
0.38627
0.27627
0.16626
0.056259
-0.053746
-0.16375
-0.27376
-0.38376
0.38882
0.27877
0.16871
0.058657
-0.051397
-0.16145
-0.2715
-0.38156

(c)

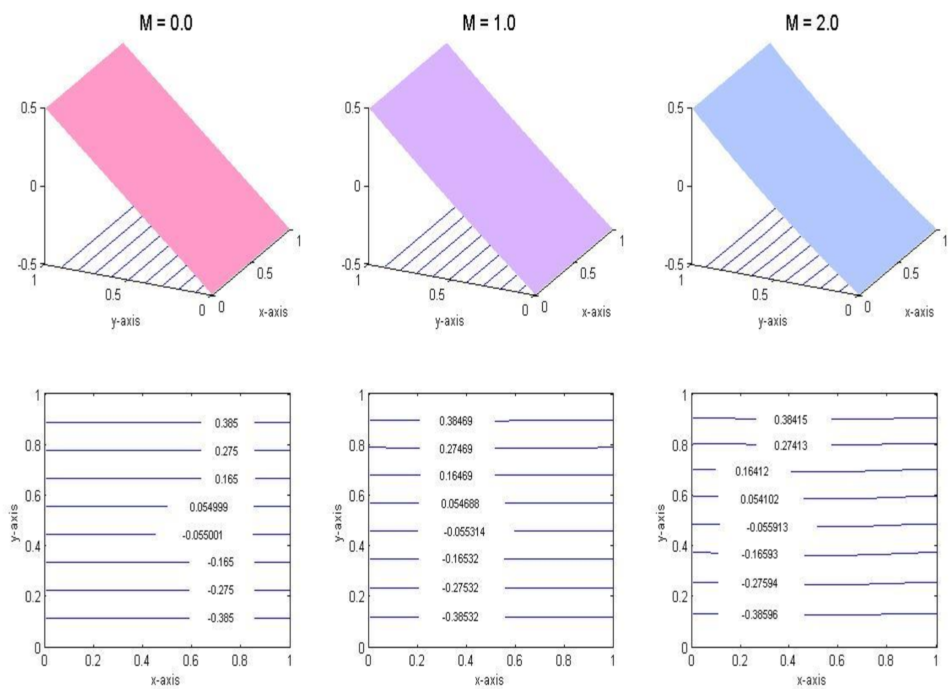

(d) **(e)** **(f)**

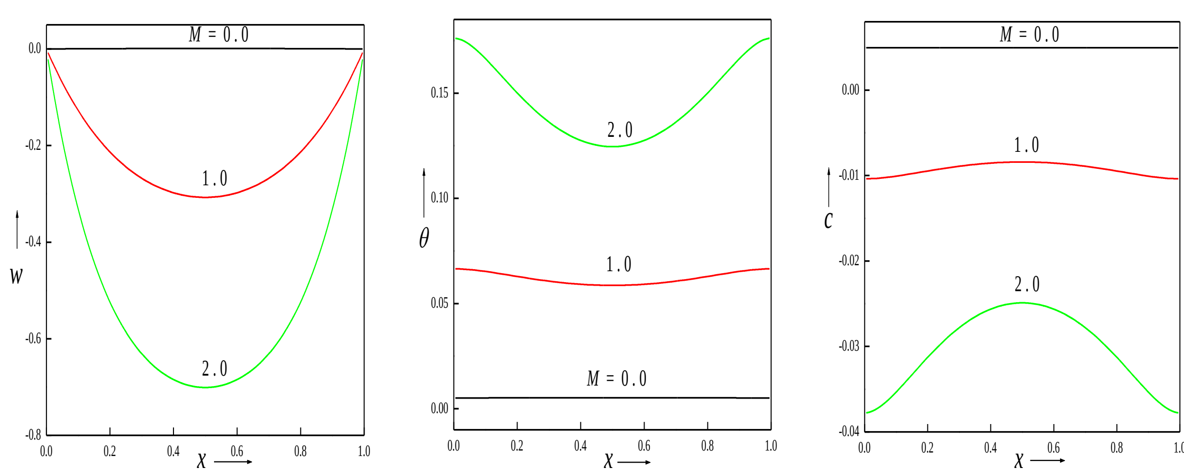

FIG. 3: Velocity (a,d), temperature (b,e) and concentration (c,f) contours and profiles respectively for different Hartmann number M

(a)

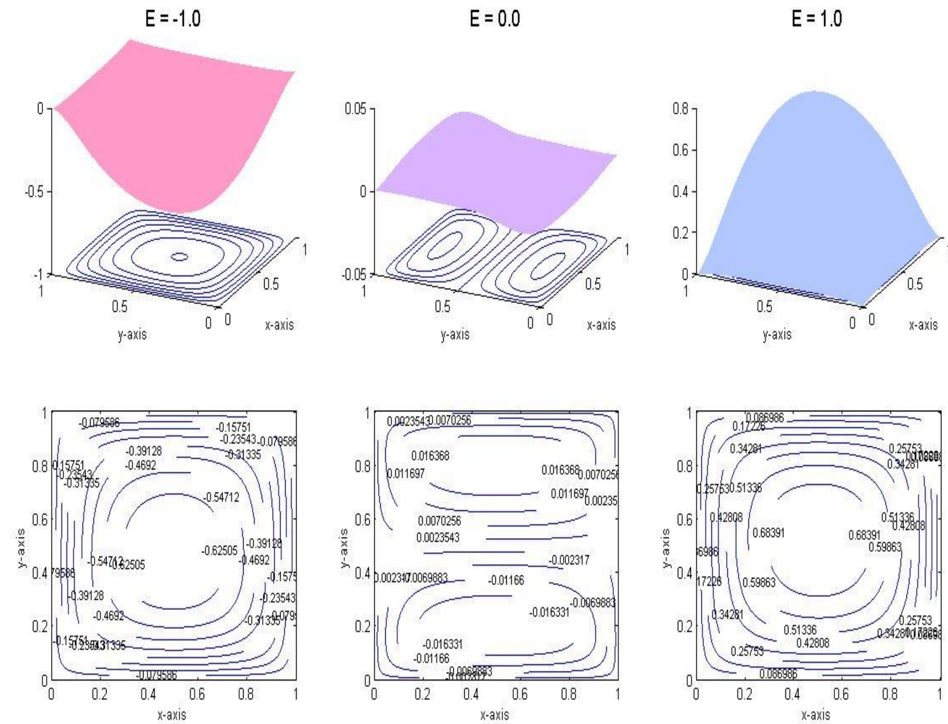

(b)

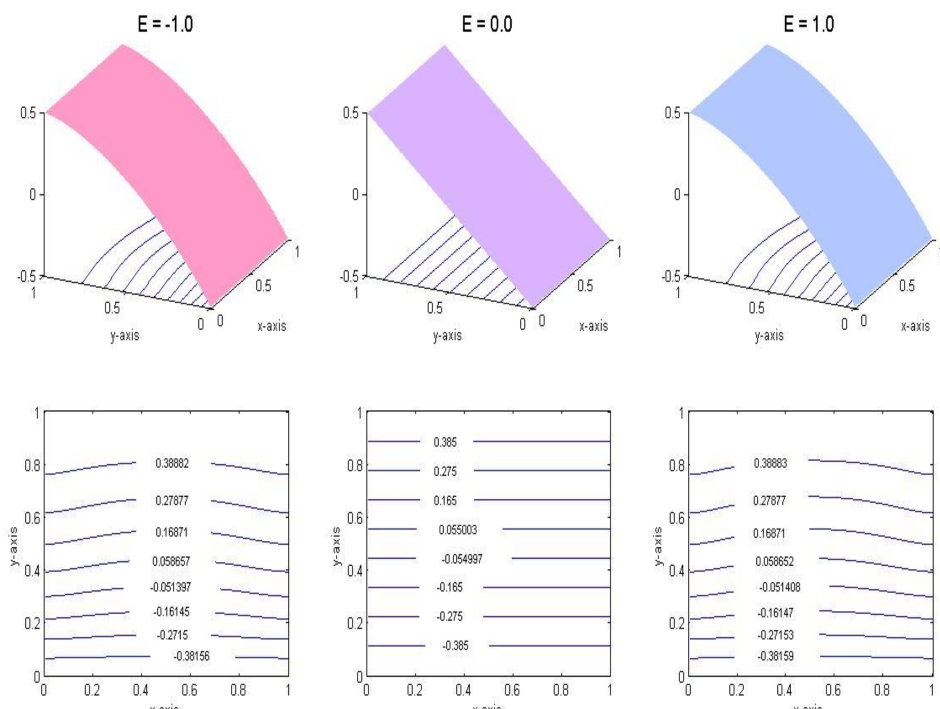

(c)

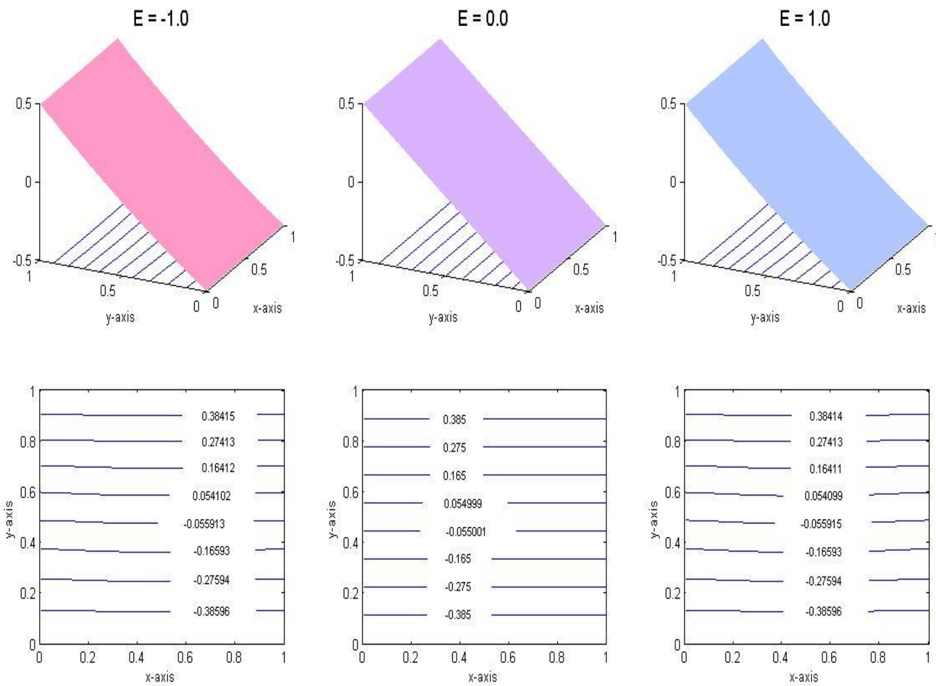

(d) **(e)** **(f)**

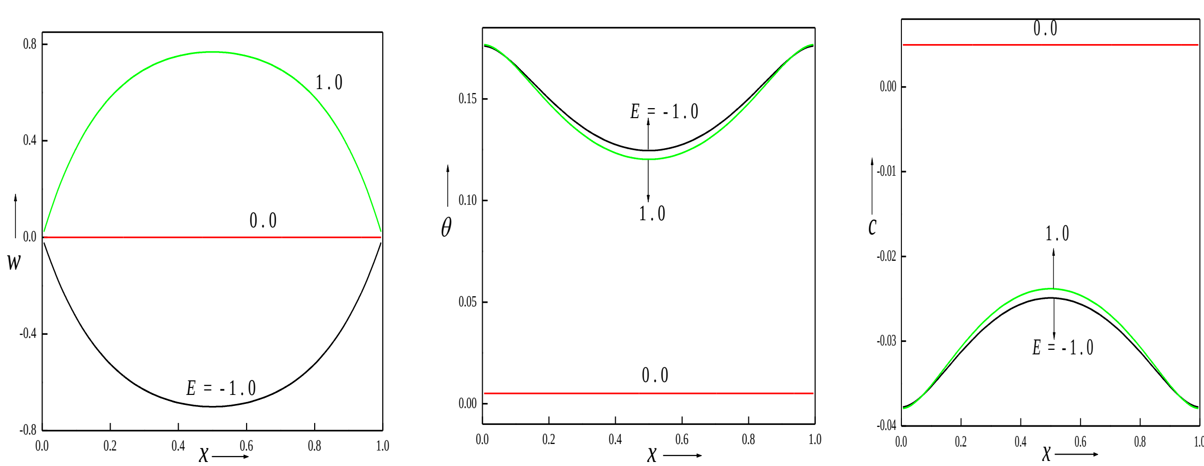

FIG. 4: Velocity (a,d), temperature (b,e) and concentration (c,f) contours and profiles respectively for different electric field load parameter E

(a)

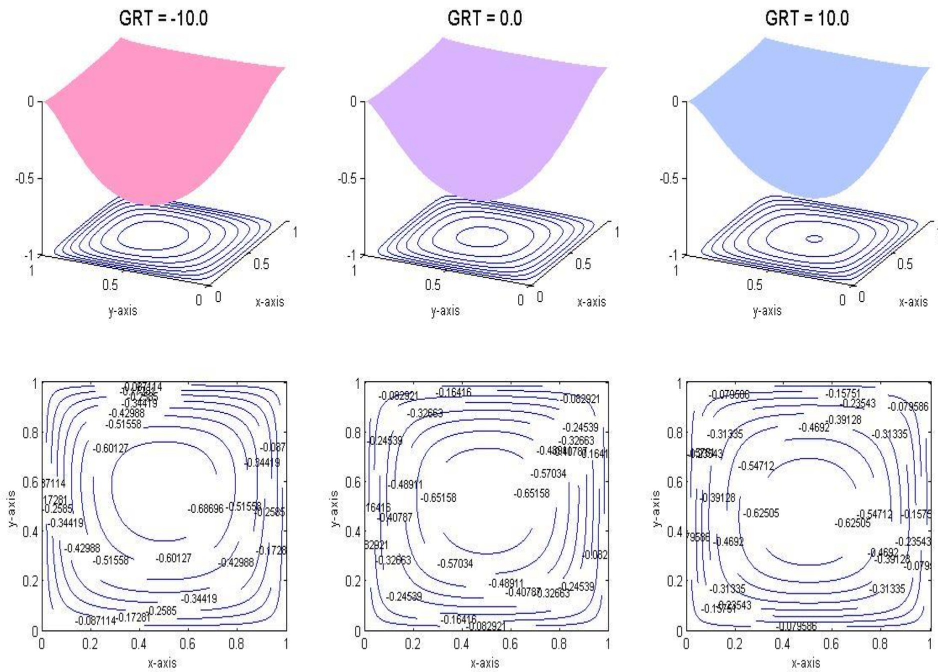
GRT = -10.0
GRT = 0.0
GRT = 10.0
y-axis
x-axis

(b)

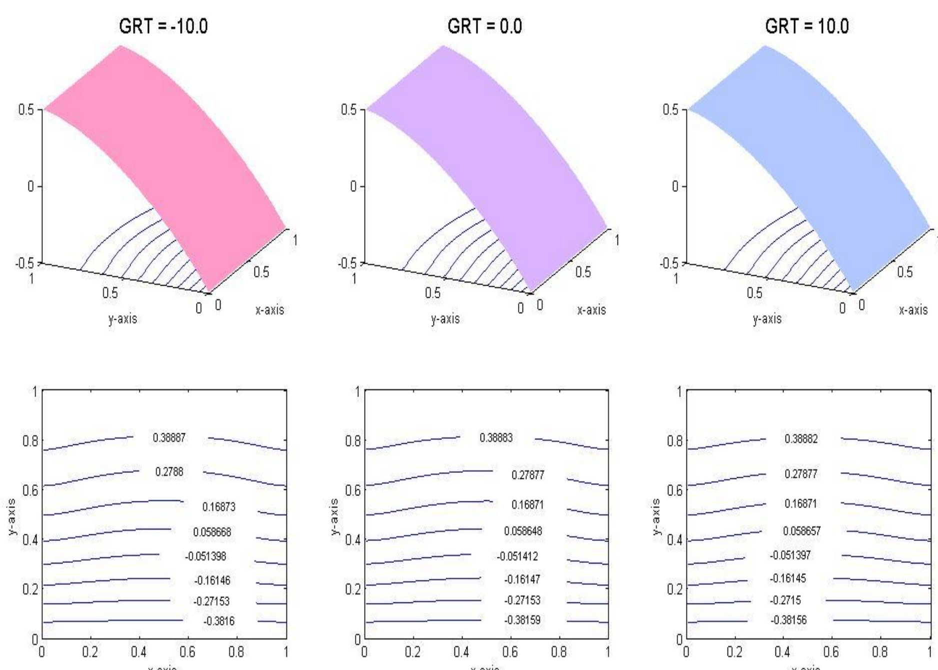
GRT = -10.0
GRT = 0.0
GRT = 10.0
y-axis
x-axis

(c)

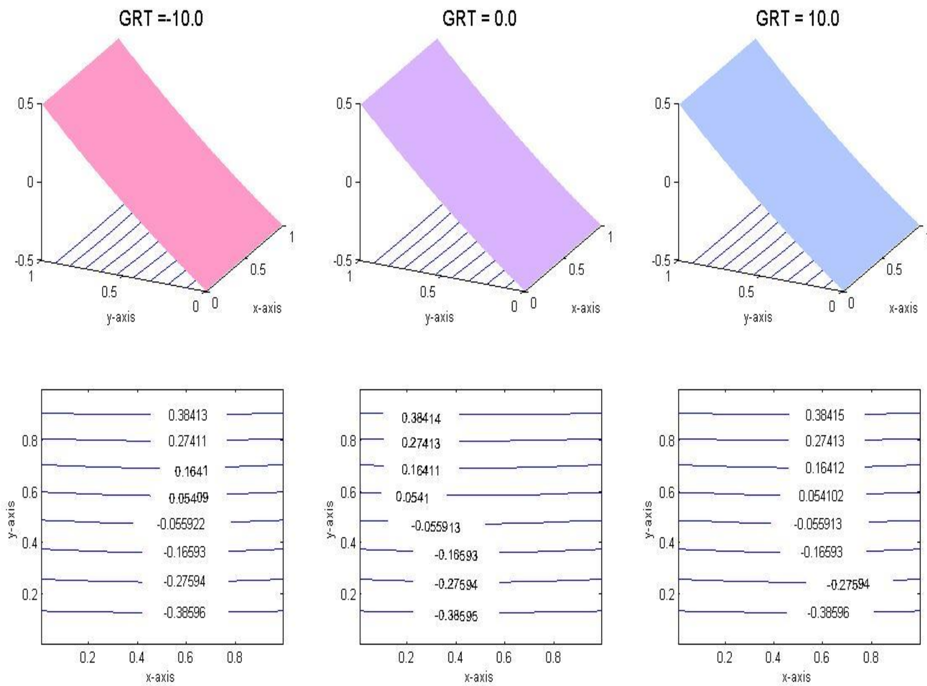

(d) **(e)** **(f)**

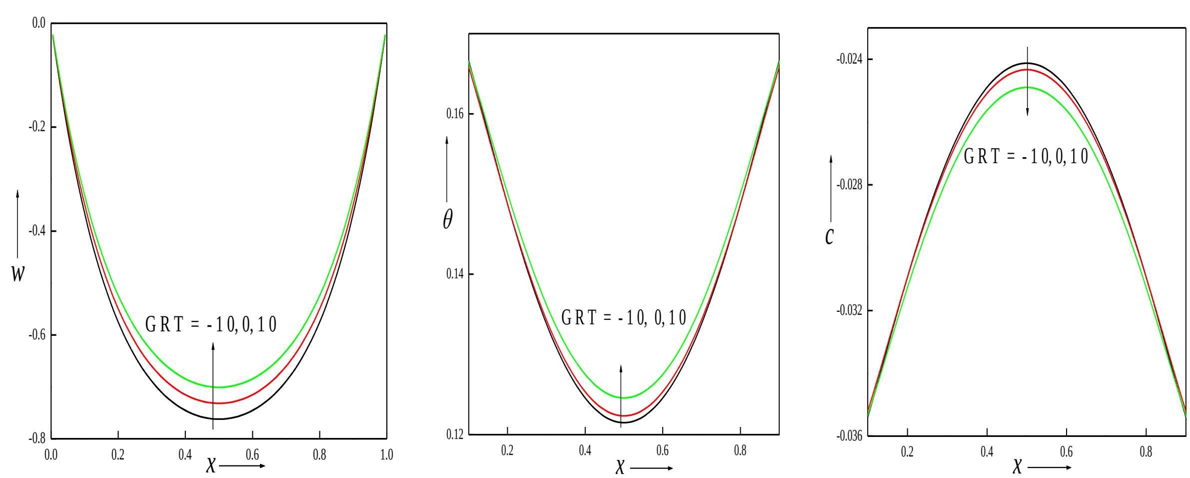

FIG. 5: Velocity (a,d), temperature (b,e)and concentration (c,f) contours and profiles respectively for different thermal Grashof number *GRT*

(a) **(b)** **(c)**

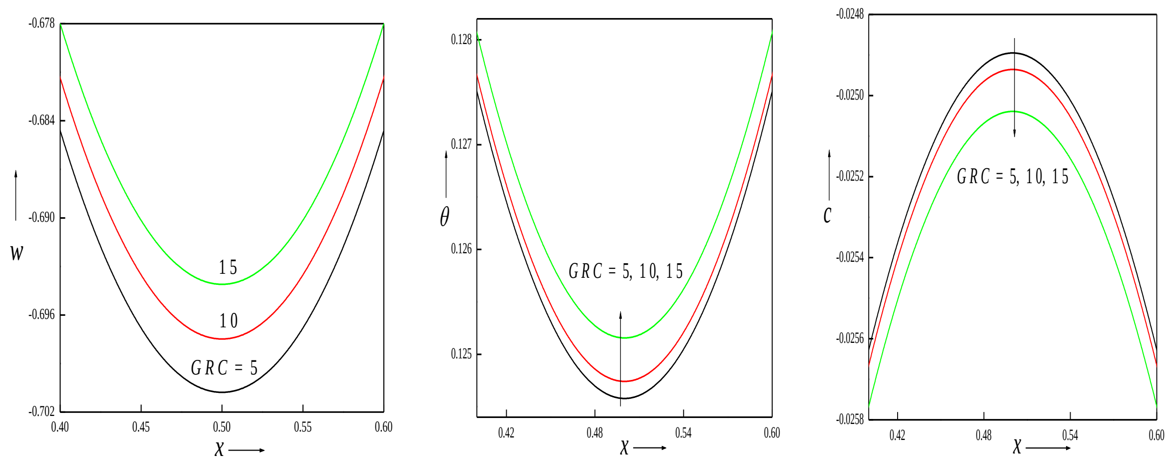

FIG. 6: Velocity (a), temperature (b) and concentration (c) profiles for different concentration Grashof number *GRC*

(a)

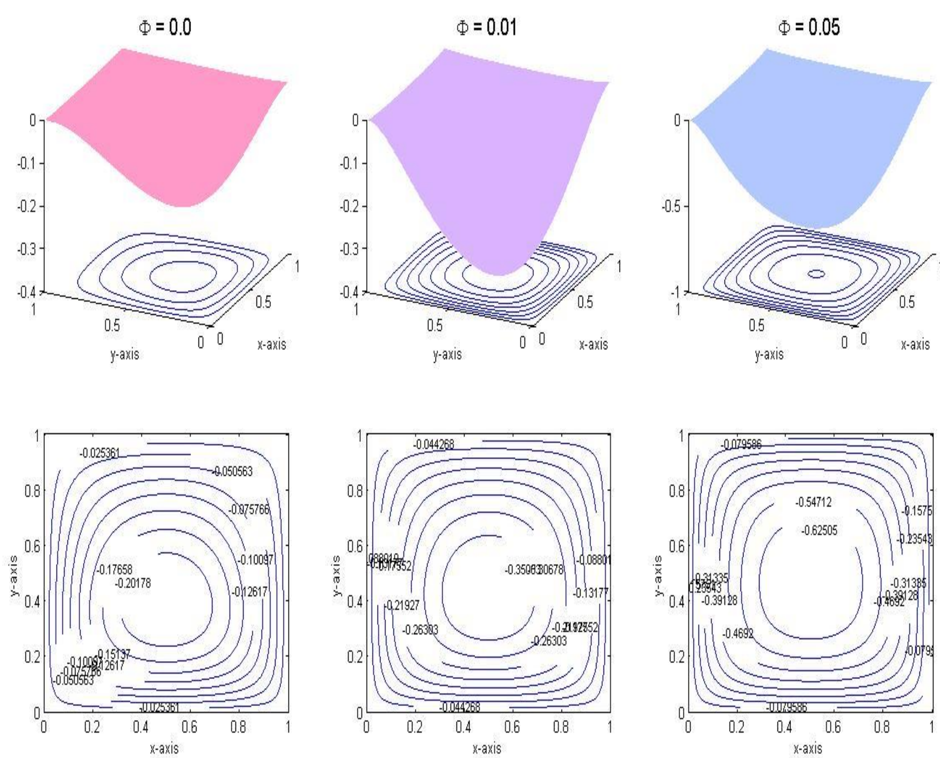

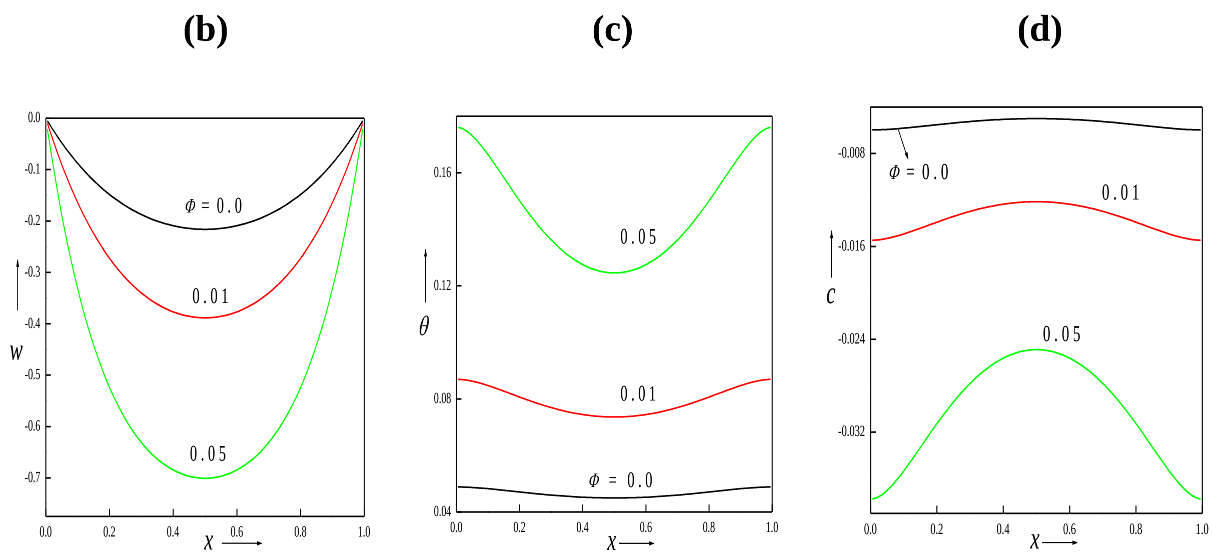

FIG. 7: Velocity (a,b), temperature (c) and concentration (d) profiles for different solid volume fraction Φ

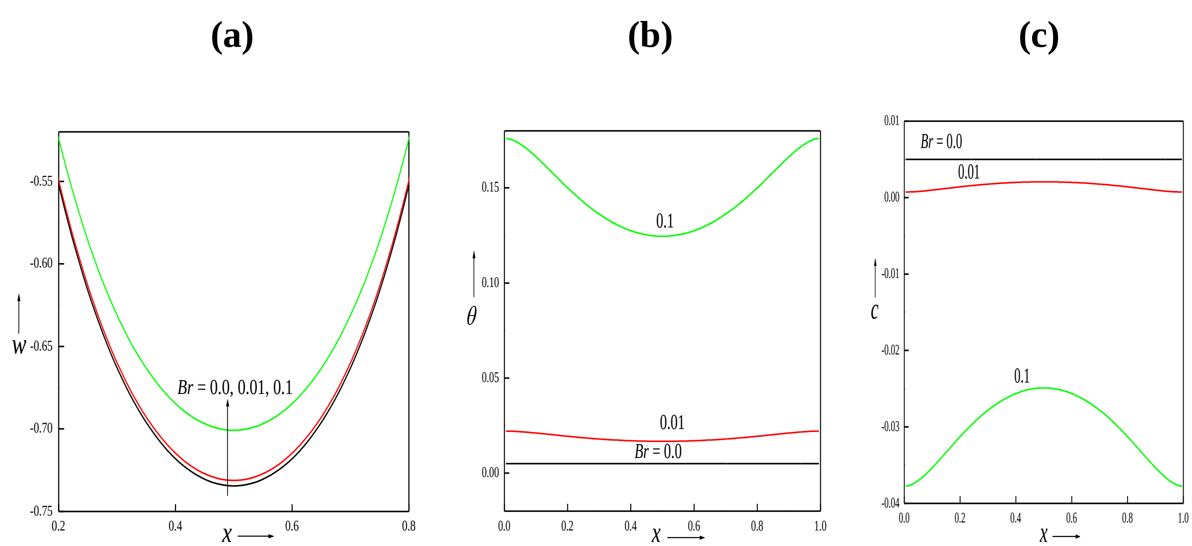

FIG. 8: Velocity (a), temperature (b) and concentration (c) profiles for different Brinkman number Br .

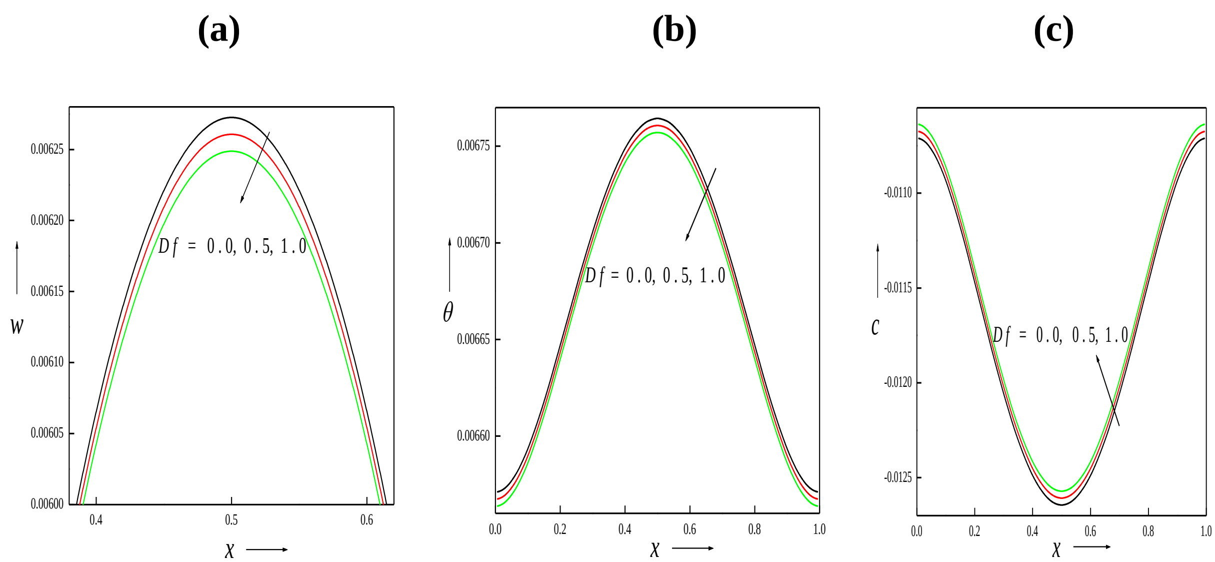

FIG. 9: Velocity (a), temperature (b) and concentration (c) profiles for different Dufour number Df

TABLE 1: Heat transfer rate and skin friction for different numerical grids

	$\left(\frac{d\theta}{dy}\right)_{y=0}$	$\left(\frac{d\theta}{dy}\right)_{y=1}$	$\left(\frac{dw}{dy}\right)_{y=0}$	$\left(\frac{dw}{dy}\right)_{y=1}$
10X10	0.58321911632	0.57310364720	-0.13011774044	-0.14335669948
50X50	0.58340390020	0.57294499882	-0.13278021128	-0.14511004150
100X100	0.58341923633	0.57294905034	-0.13287818323	-0.14515010952
150X150	0.58342960330	0.57295773078	-0.13290713985	-0.14514607580
200X200	0.58343923118	0.57296709821	-0.13292589167	-0.14513553302

TABLE 2: Volumetric flow rate and skin friction

	Q	$\left.\frac{dw}{dy}\right\|_{y=0}$	$\left.\frac{dw}{dy}\right\|_{y=1}$	$\left.\frac{dw}{dx}\right\|_{x=0}$	$\left.\frac{dw}{dx}\right\|_{x=1}$
Nano particles					
Copper	-0.38295243	-1.88736234	1.66529351	-1.73663821	1.73663821
Silver	-0.39206353	-1.94703952	1.72436713	-1.79447737	1.79447737
TiO_2	-0.24911555	-1.15611527	0.91685596	-1.01148834	1.01148834
Alumina	-0.30783274	-1.45073564	1.22119891	-1.30541565	1.30541565
M					
0.0	0.00004448	-0.13876717	-0.13899489	0.00015384	-0.00015384
1.0	-0.15364157	-0.73350049	0.47359693	-0.58826823	0.58826823
2.0	-0.38295243	-1.88736234	1.66529351	-1.73663821	1.73663821

E					
-1.0	-0.38295243	-1.88736234	1.66529351	-1.73663821	1.73663821
0.0	0.00001464	-0.11081719	-0.11089658	0.00006319	-0.00006319
1.0	0.41711761	1.75792729	-1.97938061	1.90844906	-1.90844906
GRT					
-10.0	-0.41347033	-1.52651049	2.19102068	-1.88983481	1.88983481
0.0	-0.39831336	-1.70687419	1.92862263	-1.81334029	1.81334029
10.0	-0.38295243	-1.88736234	1.66529351	-1.73663821	1.73663821
GRC					
1.0	-0.38447554	-1.98025726	1.580597179	-1.74422289	1.74422289
5.0	-0.38295243	-1.88736234	1.66529351	-1.73663821	1.73663821
10.0	-0.38102079	-1.77113131	1.77113131	-1.72704748	1.72704748
Φ					
0	-0.10710337	-0.56630533	0.26026805	-0.400627567	0.40062756
0.01	-0.19695836	-0.93868692	0.65440289	-0.77396483	0.77396483
0.05	-0.38295243	-1.88736234	1.66529351	-1.73663821	1.73663821
Br					
0	-0.40020981	-1.93372990	1.71201616	-1.82287303	1.82287303
0.01	-0.39850321	-1.92913377	1.70738886	-1.81429396	1.81429396
0.1	-0.38295243	-1.88736234	1.66529351	-1.73663821	1.73663821
Df					
0	-0.38489377	-1.89256589	1.67054134	-1.74628085	1.74628085
2.0	-0.29739629	-1.66172174	1.43679065	-1.32703175	1.32703175
5.0	-0.29739616	-1.66172141	1.43679031	-1.32703115	1.32703115

TABLE 3: Rate of heat transfer

	$\left.\frac{d\theta}{dy}\right\vert_{y=0}$	$\left.\frac{d\theta}{dy}\right\vert_{y=1}$	$\left.\frac{dc}{dy}\right\vert_{y=0}$	$\left.\frac{dc}{dy}\right\vert_{y=1}$
Nanoparticles				
Copper	0.994950	0.164485	0.410039	0.589462
Silver	1.008654	0.150857	0.407088	0.592408
TiO_2	0.810571	0.319441	0.445376	0.554211
Alumina	0.890597	0.262000	0.431475	0.568067
M				
0.0	0.579083	0.578048	0.499888	0.500111
1.0	0.724003	0.434463	0.468578	0.531133
2.0	0.994950	0.164485	0.4100397	0.589462
E				
-1.0	0.994950	0.164485	0.410039	0.589462
0.0	0.578928	0.578204	0.499921	0.500078
1.0	0.991943	0.161563	0.410689	0.590094
GRT				
-10.0	0.991218	0.155459	0.4108460	0.591412
0.0	0.991812	0.162422	0.410717	0.589908
10.0	0.994950	0.164485	0.410039	0.589462
GRC				
1.0	0.996650	0.164734	0.409672	0.589408
5.0	0.994950	0.164485	0.410039	0.589462

10.0	0.993561	0.1635713	0.410339	0.589660
Φ				
0.0	0.589342	0.411604	0.477664	0.522098
0.01	0.688403	0.343343	0.457938	0.541677
0.05	0.994950	0.164485	0.410039	0.589462
Br				
0.0	0.578566	0.578566	0.499999	0.500000
0.01	0.620181	0.537242	0.491009	0.508928
0.1	0.994950	0.164485	0.410039	0.589462
Df				
0.0	0.994873	0.164637	0.499999	0.500000
2.0	1.011746	0.144317	-3.243560	4.252798
5.0	1.011746	0.144317	-3.243564	4.252802

REFERENCES

Anwar Bég, O., Kuharat, S., Ferdows, M., Das, M., Kadir, A. and Shamshuddin, M., Magnetic nano-polymer flow with magnetic induction and nanoparticle solid volume fraction effects: solar magnetic nano-polymer fabrication simulation, *Proc. IMechE-Part N: J Nanoengineering, Nanomaterials and Nano-systems*, DOI: 10.1177/ 2397791419838714, 2019.

Aybar, H.S., Sharifpur, M., Azizian, M.R., Mehrabi, M. and Meyer, J.P., A review of thermal conductivity models for nanofluids, *Heat Transfer Engineering*, vol. 36, pp. 1085-1110, 2015.

Beghein, C., Haghighat, F. and Allard, F., Numerical study of double-diffusive natural convection in a square cavity, *Int. J. Heat and Mass Transfer*, vol. 35, pp. 833-846, 1992.

Brinkman, H.C., The viscosity of concentrated suspensions and solutions, *J. Chem. Physics*, vol. 20, pp. 571-581, 1952.

Buongiorno, J., Convective transport in nanofluids, *ASME J. Heat Transfer*, vol. 128, pp. 240-250, 2006.

Diglio, G., Roselli, C., Sasso, M. and Umavathi, J.C., Borehole heat exchanger with nanofluids as heat carrier, *Geothermics*, vol. 72, pp. 112-123, 2018.

Lee, J.W. and Hyun, J.M., Double-diffusive convection in a rectangle with opposing horizontal temperature and concentration gradients, *Int. J. Heat and Mass Transfer*, vol. 33, pp. 1619-1632, 1990.

Malashetty, M.S., Umavathi, J.C. and Prathap Kumar, J., Magnetoconvection of two-immiscible fluids in a vertical enclosure, *Heat Mass Transfer*, vol. 42, pp. 977-993, 2006.

Maxwell, J.C., A *Treatise on Electricity and Magnetism*, 2nd ed. Oxford Cambridge, UK : Oxford University Press, 1904.

Minea, A.A., Uncertainties in modeling thermal conductivity of laminar forced convection heat transfer with water alumina nanofluids, *Int. J. Heat and Mass Transfer*, vol. 68, pp. 78-84, 2014.

Sharma, P.R. and Singh, G., Effects of Ohmic heating and viscous dissipation on steady MHD flow near a stagnation point on an isothermal stretching sheet, *Thermal Science*, vol. 13, pp. 5-12, 2009.

Sheikholeslami, M., Hatami, M. and Ganji, D.D., Analytical investigation of MHD Nanofluid flow in a semi-porous channel, *Powder Technology*, vol. 246, pp. 327-336, 2013.

Ting, T.W., Hung, Y.M. and Guo, N., Field-synergy analysis of viscous dissipative nanofluid flow in microchannels, *Int. J. of Heat Mass Transfer*, vol. 73, pp. 483-491, 2014.

Trevisan, O. and Bejan, A., Combined heat and mass transfer by natural convection in a vertical enclosure, *ASME J. Heat Transfer*, vol. 109, pp. 104-112, 1987.

Uddin, M.J., **Anwar, Bég, O**., Ghose, P.K. and Ismael, A.I.M., Numerical study of non-Newtonian nanofluid transport in a porous medium with multiple convective boundary conditions and nonlinear thermal radiation effects, *Int. J. Num. Meth. Heat Fluid Flow*, vol. 26, pp. 1-25, 2016.

Umavathi, J.C., Effect of thermal modulation on the onset of convection in a porous medium layer saturated by a nanofluids, *Transport Porous Media*, vol. 98, pp. 59-79, 2013b.

Umavathi, J.C. and Chamkha, A.J., Mixed convection flow of an electrically conducting fluid in a vertical channel with boundary conditions of the third kind, *Canadian Journal of Physics*, vol. 92, pp. 1387-1396, 2014a.

Umavathi, J.C. and Sheremet, M.A., Influence of temperature dependent conductivity of a nanofluid in a vertical rectangular duct, *Int. J. Nonlinear Mechanics*, vol. 78, pp. 17-28, 2016c.

Umavathi, J.C. and Liu, I.C., Magnetoconvection in a vertical channel with heat source or sink, *Meccanica*, vol. 48, pp. 2221-2232, 2013a.

Umavathi, J.C. and Mohite, M.B., The onset of convection in a nanofluid saturated porous layer using Darcy model with cross diffusion, *Meccanica,* vol. 49, pp. 1159-1175, 2014c.

Umavathi, J.C., Odelu Ojjela, Vajravelu, K., Numerical analysis of natural convective flow and heat transfer of nanofluids in a vertical rectangular duct using Darcy-Forchheimer-Brinkman model, *Int. J. Thermal Sciences*, vol. 11, pp. 511-524, 2017c.

Umavathi, J.C. and Prathap Kumar, J., Onset of convection in a porous medium layer saturated with an Oldroyd nanofluid, *ASME. J. Heat Transfer*, vol. 139, pp. 012401-1-14, 2017a.

Umavathi, J.C., Sasso, M., Free convection flow in a duct filled with nanofluid and saturated with porous medium: Variable properties, *Journal of Porous Media*, vol. 9, pp. 155-176, 2018.

Umavathi, J.C., Sasso, M. and Prathap Kumar, J., Effect of first order chemical reaction on magneto convection of immiscible fluids in a vertical channel, *Advances in Mathematics and Computer Science and their Applications*, pp. 32-39, 2016a.

Umavathi, J.C., Prathap Kumar, J. and Sheremet, M.A., Heat and mass transfer in a vertical double passage channel filled with electrically conducting fluid, *Physica-A*, vol. 465, pp. 195-216, 2017c.

Umavathi, J.C., Liu, I.C. and Sheremet, M.A., Convective heat transfer in a vertical rectangular duct filled with a nanofluid, *Heat Transfer Asian Research*, vol. 45, pp. 661-679, 2016b.

Umavathi, J.C., Liu, I.C., Prathap Kumar, J. and Pop, I., Fully developed magneto convection flow in a vertical rectangular duct, *Heat Mass Transfer*, vol. 47, pp. 1-11, 2011.

Vadher, P.A., Deheri, G.M. and Patel, R.M., Performance of hydromagnetic squeeze films between conducting porous rough conical plates, *Meccanica*, vol. 45, pp. 767-783, 2010.

Wang, J., Yang, M. and Zhang, Y., Onset of double-diffusive convection in horizontal cavity with Soret and Dufour effects, *Int. J. Heat Mass Transfer*, vol. 78, 1023-1031, 2014.

Wang, X.Q. and Mujumdar, A.S., Heat transfer characteristics of nanofluids: A Review, *Int. J. Thermal Sciences*, vol. 46, pp. 1-19, 2007.

Xuan, Y. and Li, Q., Investigation on convective heat transfer and flow features of nanofluids, *ASME J. Heat Transfer*, vol. 125, pp. 151-155, 2003.

Younsi, R., Computational analysis of MHD flow, heat and mass transfer in trapezoidal porous cavity, *Thermal Science*, vol. 13, pp. 13-22, 2009.

Yu, W., France, D.M., Routbort, J.L. and Choi, S.U.S., Review and comparison of nanofluid thermal conductivity and heat transfer enhancements, *Heat Transfer Engineering*, vol. 29, pp. 432-460, 2008.